

A Charge-Noise Insensitive Chiral Photonic Interface for Waveguide Circuit QED

Yu-Xiang Zhang,^{1,*} Carles R. i Carceller,² Morten Kjaergaard,³ and Anders S. Sørensen¹

¹*Center for Hybrid Quantum Networks (Hy-Q), The Niels Bohr Institute, University of Copenhagen, Blegdamsvej 17, 2100 Copenhagen Ø, Denmark*

²*Department of Physics, Technical University of Denmark, Fysikvej 307, 2800 Kgs. Lyngby, Denmark*

³*Center for Quantum Devices, Niels Bohr Institute, University of Copenhagen, 2100 Copenhagen Ø, Denmark*

(Dated: December 2, 2021)

A chiral photonic interface is a quantum system that has different probabilities for emitting photons to the left and right. An on-chip compatible chiral interface is attractive for both fundamental studies of light-matter interactions and applications to quantum information processing. We propose such a chiral interface based on superconducting circuits, which has wide bandwidth, rich tunability, and high tolerance to fabrication variations. The proposed interface consists of a core that uses Cooper-pair-boxes (CPBs) to break time-reversal symmetry, and two superconducting transmons which connect the core to a waveguide in the manner reminiscent of a “giant atom”. The transmons form a state decoupled from the core, akin to dark states of atomic physics, rendering the whole interface insensitive to the CPB charge noise. The proposed interface can be extended to realize a broadband fully passive on-chip circulator for microwave photons.

The emission of photons from quantum systems is typically non-chiral, meaning that the emitted photons have equal probability to propagate in opposite directions. The opposite situation, where the emitted photons propagate in a single direction, allows for a wide range of novel phenomena including cascaded driven-dissipative dynamics [1, 2], spin dimers [3, 4], photonic bound states [5–7], and solvable models of waveguide quantum electrodynamics (QED) [8]. Chiral interfaces enabling the study of such effects have recently been developed for optical photons [9], but optical systems are prone to losses, limiting the quality of the interfaces. In comparison, superconducting circuits realize almost ideal interfaces to guided microwave photons [10–12], potentially allowing for much cleaner demonstrations of these fundamental effects, but so far no chiral interactions have been realized for these systems.

Chiral interfaces to superconducting systems are also of immense technological interest. Scaling superconducting quantum computers to larger sizes puts high demands on the ability to route signals between different components on the chips, e.g., using circulators. Such circulators necessarily break Lorentz reciprocity and thereby time-reversal symmetry (TRS). Commercially available circulators often exploit the Faraday effect [13]. However, such components are off-chip, requiring additional space inside the experimental apparatus. Most of the existing proposals for on-chip circulators break TRS by tailored active control [10, 14–23], e.g., via a synthetic magnetic field [22], or by dynamically modulating switches and delays [23]. On-chip circulators that can be operated in a passive form, thereby simplifying its experimental implementations, however remain elusive. A Josephson junction ring threaded by a constant magnetic flux breaks TRS [24], but its applicability as a circulator in current superconducting hardware is challenging,

because the system must be operated in the Cooper-pair-box (CPB) regime [24–26] which is susceptible to charge noise [11, 27] and limited by bandwidth and fabrication variations [28]. The bandwidth can, however, be increased substantially by exploiting carefully engineered circuits with high impedance [29].

In this Letter, we develop an on-chip tunable broadband charge-insensitive chiral system illustrated in Fig. 1(a). The system is designed such that the (non-degenerate) excited states decay by only emitting photons in one direction, left or right. It has a core composed of two CPBs and an applied external flux (green box), and two transmons that connect the core to the waveguide at two separated locations, being reminiscent of a “giant atom” [30–32]. The core is essential for breaking TRS, while the transmons amplify the coupling to the waveguide and hence the bandwidth. Furthermore, by operating in a particular dark state configuration [33] we show that excitation of the CPBs can be suppressed, such that the interface maintains the excellent coherence properties of transmons [34, 35], while still exploiting the inherent breaking of TRS by the CPBs. The interface can directly be extended to realise a circulator for routing signals in large scale superconducting devices. Finally, the tunability of our chiral interface allows compensating fabrication variations as well as control of the operating frequency within a range of a few GHz.

Recent related proposals [36, 37] have used giant atoms formed by transmons and careful adjustments of parameters to realize unidirectional interactions with two degenerate levels, which decay in opposite directions. This degeneracy means that TRS is not broken, and the additional level provides a complication of the dynamics, in particular for non-perfect or partially chiral systems. Compared to these works, our chiral interface realizes the paradigmatic chiral model of a two-level system with chi-

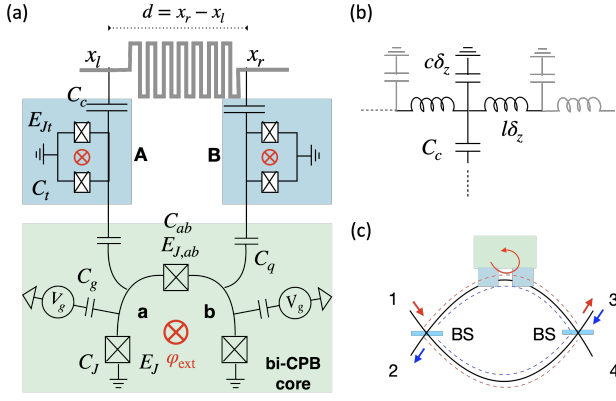


Figure 1. Proposal for realizing on-chip compatible charge-noise insensitive chiral photonic interface. (a) Circuit of the chiral interface consisting of two CPBs (green boxes) coupled to a waveguide (top) through two tunable transmons (blue boxes) connecting to the waveguide at positions x_l and x_r . C_J and E_J denotes the capacitance and Josephson energy of the CPBs, C_{ab} and $E_{J,ab}$ are those of the junction connecting CPB-a and CPB-b, φ_{ext} is the dimensionless external flux, C_g is the gate capacitance, C_q couples the CPB and transmons, C_t and E_{Jt} are the total capacitance and (tunable) Josephson energy of the transmons and C_c couples the transmons to the transmission line. (b) Circuit model of the capacitive coupling between a transmon and the transmission line. (c) A circulator based on chiral interface (right-hand chirality) and Mach-Zehnder interferometer. “BS” denotes 50:50 beam splitters. Input from port-1 goes to port-3 while input from port-3 goes to port-2.

ral coupling, has tunable operating frequency, and more importantly, can be used for photonic circulators. During the final stages of this work, a different proposal suggested a chiral interface based on a specially designed waveguide and active driving [38].

Preliminaries. We first consider two coupled CPBs, “a” and “b”, which as a whole, has the ground state $|g_{ab}\rangle$ and a non-degenerate excited state $|e\rangle$. The tran-

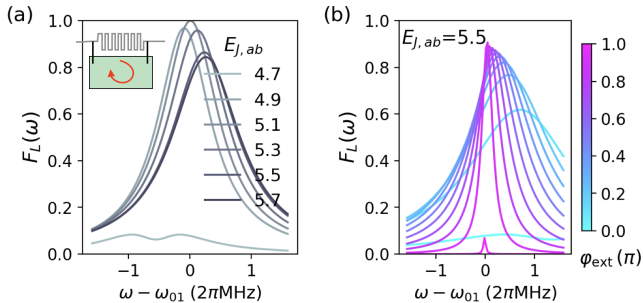


Figure 2. Fidelity of circulator $F_L(\omega)$ against the detuning to the first excited state for direct coupling between the waveguide and the bi-CPB core. The device parameters are: $c\delta_z = C_q = C_\Sigma = C_{ab} = 1\text{fF}$, $E_J = 5.5\text{ hGHz}$, and (a) $\varphi_{ext} = 0.5\pi$ and various values of $E_{J,ab}$ (hGHz); (b) $E_{J,ab} = 5.5\text{ hGHz}$ and the external flux φ_{ext} varying from 0 to π .

sition between them is resonant with waveguide modes of wavenumber $\pm k_0$. We couple CPB-a and CPB-b to the waveguide at positions x_l and x_r , respectively [see Fig. 1(a)], resulting in coupling operators of the form $\hat{a}_{\pm k_0}(\hat{n}_a + e^{\pm ik_0 d}\hat{n}_b)$, where $\hat{a}_{\pm k_0}$ is the photon annihilation operator, $d = x_r - x_l$ and $\hat{n}_{a/b}$ is the CPB charge number operator. Within the rotating-wave approximation and perturbation theory, the decay from $|e\rangle$ to left/right going photons depends on the magnitude of

$$\lambda_{\pm} = \eta_a + e^{\pm ik_0 d}\eta_b, \quad \eta_{a/b} = \langle e|\hat{n}_{a/b}|g_{ab}\rangle. \quad (1)$$

This formula expresses the interference between excitation decaying through the left and right arms in Fig. 2(a), which depends on both the coupling matrix element $\eta_{a/b}$ at x_l/r and the phase $e^{\pm ik_0 d}$ from waveguide propagation between them.

A chiral interface with a single excited state requires TRS to be broken since left and right propagation are connected by TRS, and a state invariant under TRS cannot distinguish these two possibilities. Breaking of TRS, however, may induce a phase difference between η_a and η_b allowing the cancellation of λ_+ or λ_- for a suitable $k_0 d$ if $|\eta_a| = |\eta_b|$.

Incorporating the chiral interface into one of the arms of a balanced Mach-Zehnder interferometer enables the construction of a four-port photonic circulator [Fig. 1(c)]. Suppose the scattering matrix of the chiral interface is $S_{\epsilon\epsilon'}(\omega_k)$ with $\epsilon, \epsilon' = \pm 1$ denoting the matrix element from wavenumber $\epsilon'k$ to ϵk . If the interface has ideal right-hand chirality, there will be no phase shift for the uncoupled left-moving photons ($S_{--} = 1$), whereas a π phase shift is attained for the perfectly coupled right-moving photons ($S_{++} = -1$). This phase difference of π implies that the Mach-Zehnder interferometer, shown in Fig. 1(c), can be balanced such that a right-moving photon incident in Port-1 exits through Port-3, whereas a left-moving photon incident in Port-3 exits through Port-2, realizing a circulator. We define the fidelity of the circulator as the product of the probabilities for these two inputs to exit through the correct port, which is given by

$$F_{R/L}(\omega) = \frac{1}{16} |1 \mp S_{++}(\omega)|^2 |1 \pm S_{--}(\omega)|^2. \quad (2)$$

Obviously $F_{R/L} = 1$ if $S_{++} = \mp 1$ and $S_{--} = \pm 1$. In the Supplemental Material [39] we show the system Hamiltonian and use the input-output formalism to derive the scattering matrix, based on which the fidelity (2) can be numerically evaluated for given setups.

The bi-CPB core. TRS can be broken by Josephson junction rings threaded by magnetic flux [24]. Here we use an equivalent “bi-CPB core” [39] depicted in the green box of Fig. 1(a). It has two CPBs denoted by “a” and “b”, which are assumed identical for now. Each CPB has a junction with Josephson energy E_J and capacitance C_J . The voltage source determines the offset charge $n_{g,a/b}$ through a capacitor with capacitance

C_g . We define $C_\Sigma = C_J + C_g$. The two CPBs are connected by a Josephson junction with capacitance C_{ab} and Josephson energy $E_{J,ab}$. The external flux φ_{ext} is made dimensionless by expressing it in units of $\Phi_0/(2\pi)$ with Φ_0 being the flux quantum. As depicted in Fig. 1(b), the transmission line waveguide is modeled by an infinite chain of coupled LC-oscillators with capacitance $c\delta_z$ and inductance $l\delta_z$. The waveguide parameters are set by realistic impedance $Z = \sqrt{l/c} = 50\Omega$ and the speed of light $v_g = 1/\sqrt{l/c} \approx 1.2 \times 10^8 \text{m/s}$. The elementary length, δ_z , is determined by the lateral size of the coupling capacitor C_c (or C_q if using only the bi-CPB core).

At first, we consider coupling the bi-CPB core directly to the waveguide at $x_{l/r}$, with device parameters given in the caption of Fig. 2. Particularly, we set $c\delta_z = 1\text{fF}$ corresponding to $\delta_z \approx 5\mu\text{m}$, which is comparable to the size of typical CPBs [25]. To suppress the dephasing caused by charge noise, the offset charge $n_{g,a/b}$ is fixed at the ‘‘sweet spot’’ where $\partial\omega_{01}/\partial n_g = 0$ [40] and ω_{0n} is the energy gap between the n th excited state and the ground state of the core (the sweet spot $n_{g,a/b} = 0.5$ must be excluded, because here particle-hole symmetry preserves TRS). The separation $d = x_r - x_l$ is selected so that $k_0d = \pi/2$.

In Fig. 2(a), we plot $F_L(\omega)$ as a function of detuning from ω_{01} for $\varphi_{\text{ext}} = 0.5\pi$ and a few values of $E_{J,ab}$. The plot shows that the bare core can indeed acts as a chiral emitter, but suffers from several shortcomings. Firstly, the peak fidelity, $\max_\omega F_{R/L}(\omega)$, is sensitive to the exact value of $E_{J,ab}$, leaving the device performance highly sensitive to fabrication variation. Fabrication variations might be compensated by adapting the tunable flux φ_{ext} . To examine this, we choose a representative $E_{J,ab} = 5.5 \text{hGHz}$ corresponding to a 10% deviation from the ideal value and plot $F_L(\omega)$ as a function of φ_{ext} in Fig. 2(b). It shows that this tuning fails to make the maximal fidelity above 0.9. Furthermore, tuning φ_{ext} changes ω_{01} , rendering this configuration inadequate for tasks where photon frequencies are fixed. Figure 2 also shows that the bandwidth is less than 1MHz, which severely limits the functionality.

The transmon-coupled bi-CPB chiral photonic interface. The bandwidth is limited by the weak interaction between the small CPBs and the waveguide excitations delocalized on wavelength scale. To overcome this, we propose to insert transmons, which have lateral size in between the CPBs and the photonic wavelength, as efficient mediators. Compared with similar proposals using microwave resonators [27, 29], transmons allow for stronger spatial confinement of excitations, and thereby larger couplings to the CPBs, while simultaneously maintaining sizable coupling to waveguides. A similar advantage could be achieved with high impedance elements [29], but the transmons additionally allow wide tunability as discussed below. In Fig. 3(a) we plot $F_{R/L}(\omega)$ as a function of the detuning to the first two excited states

(ω_{01} and ω_{02}) for the CPB-transmon-coupled system. The device parameters used in the calculation are listed in Fig. 3(c), which are chosen to be representative for typical experimental situations and not fully optimized. Particularly, we have taken $c\delta_z = 50\text{fF}$ i.e., $\delta_z \approx 250\mu\text{m}$, corresponding to the lateral size of the transmon reported in Ref. [41]. Figure 3(a) shows that the bandwidth is significantly improved. However, while a left-hand chirality ($F_L \gg F_R$) is realized for $\omega \approx \omega_{01}$ (and $\omega \approx \omega_{03}$) – similar to the bare bi-CPB core – we observe the opposite chirality for $\omega \approx \omega_{02}$ ($F_R \gg F_L$). This feature indicates the distinctness of the 2nd excited state. Below we use an approximate model to highlight multiple benefits brought by this state.

We assume that the two transmons, indexed by ‘‘A’’ and ‘‘B’’ in Fig. 1(a), are identical in parameters, and consider a restricted Hilbert space spanned by the ground state and the singly-excited states of either transmon-A,B, or the bi-CPB core, which will be denoted by $|1_A\rangle$, $|1_B\rangle$, and $|e\rangle$, respectively. The device Hamiltonian reads $H = H_0 + H_{\text{int}}$, where $H_0 = e_1 |e\rangle \langle e| + \omega_t (|1_A\rangle \langle 1_A| + |1_B\rangle \langle 1_B|)$ with e_1 and ω_t the energies of the 1st excited states of the core and the transmons, respectively. The interaction Hamiltonian is

$$H_{\text{int}} = g\hat{n}_A(\hat{n}_a - n_{g,a}) + g\hat{n}_B(\hat{n}_b - n_{g,b}), \quad (3)$$

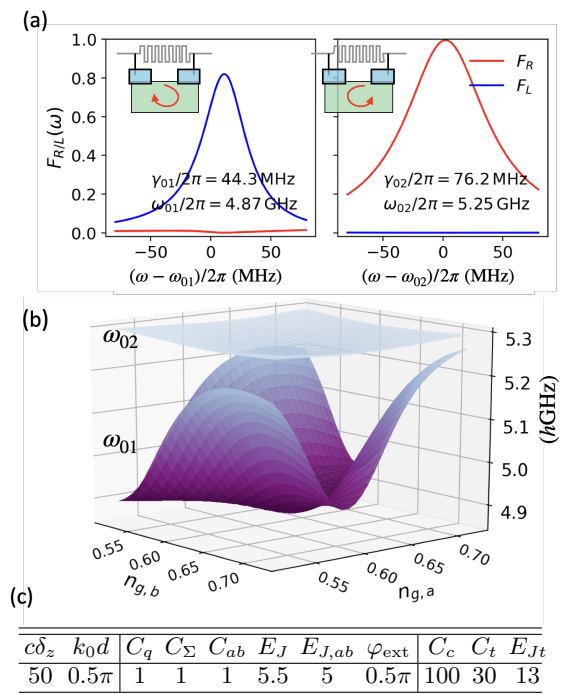


Figure 3. Energy levels and performance of the full system. (a) Fidelity of circulator as a function of the detuning from ω_{01} and ω_{02} with device parameters in (c). (b) Values (in unit of hGHz) of ω_{01} and ω_{02} of the full device as a function of $n_{g,a/b}$, using parameters listed in (c), where units for capacitances and Josephson energies are fF and hGHz , respectively.

where g is the coupling strength. Using rotating-wave approximation upon H_{int} , and restricting it to the reduced Hilbert space, we rewrite H as

$$H = H_0 + \tilde{g}(|\psi_c\rangle\langle e| + |e\rangle\langle\psi_c|), \quad (4)$$

where \tilde{g} is modified from g and

$$|\psi_c\rangle \propto \eta_a^* |1_A\rangle + \eta_b^* |1_B\rangle, \quad (5)$$

with $\eta_{a(b)} = \langle e|\hat{n}_{a(b)}|g_{ab}\rangle$ as in Eq. (1). The coupling between $|\psi_c\rangle$ and $|e\rangle$ yields the 1st excited state $|\Psi_-\rangle$ with energy $\omega_{01} = e_1 + \Delta_-$ and the 3rd excited state $|\Psi_+\rangle$ with energy $\omega_{03} = e_1 + \Delta_+$,

$$|\Psi_{\pm}\rangle \propto \underbrace{\Delta_{\pm} |\psi_c\rangle}_{\text{transmons}} + \underbrace{i\tilde{g} |e\rangle}_{\text{bi-CPB}} \quad (6)$$

where $\Delta_{\pm} = -\delta/2 \pm \sqrt{\delta^2/4 + \tilde{g}^2}$ with $\delta = e_1 - \omega_t$. The 2nd excited state is a so-called dark state [33], which has no excitation on the core,

$$|\Psi_{\text{de}}\rangle \propto \eta_b |1_A\rangle - \eta_a |1_B\rangle. \quad (7)$$

Despite being decoupled, $|\Psi_{\text{de}}\rangle$ still attains chiral property from the core. The constants $\eta_{a(b)}$, however, have different orders and signs in $|\Psi_{\text{de}}\rangle$ and $|\psi_c\rangle$, which lead to opposite chirality.

A more important observation is that the state $|\Psi_{\text{de}}\rangle$ does not contain the bi-CPB state $|e\rangle$. Thus, it is not affected by the CPB charge noise and keeps the charge noise insensitivity of the transmon qubits [27]. To illustrate this, Fig. 3(b) shows ω_{01} and ω_{02} as a function of the offset charges $n_{g,a/b}$. The results are numerically evaluated from the complete Hamiltonian (see [39] for details) using device parameters listed in Fig. 3(c). Figure 3(b) demonstrates that ω_{02} is significantly more stable than ω_{01} . The fluctuation of ω_{02} does not exceed its linewidth $\gamma_{02}/2\pi \approx 76$ MHz despite the large variations in $n_{g,a/b}$. Thus, the offset charges $n_{g,a(b)}$ need not be at the sweet spots, and can be used as control knobs to provide tunability.

Tunability of the chiral interface. First, we demonstrate that by tuning $n_{g,a/b}$ and φ_{ext} we can address issues of fabrication variation in the device parameters. To simulate realistic fabrication variations, we sample values of capacitance and CPB Josephson energy uniformly in intervals bounded by $\pm 1\%$ and $\pm 10\%$, respectively, from the intended values listed in Fig. 3(c). The transmon Josephson energy E_{Jt} is fixed at the intended values because they can be tuned *in situ* via flux-control. We collect 150 such “realistic samples”, which includes cases with asymmetries between CPB-a and CPB-b, and between transmon-A and transmon-B. In Fig. 4(a), we fix $n_{g,a/b}$ and φ_{ext} at the optimal value for the ideal parameters, and show by grey points their individual maximal fidelity (vertical coordinate), frequency where the maximal fidelity is obtained (horizontal coordinate), and

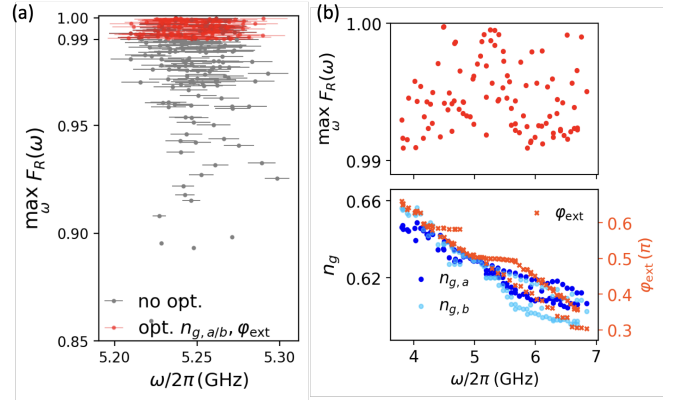


Figure 4. Tunability of the chiral interface. (a) 150 realizations of the chiral interfaces with device parameters randomly sampled to represent fabrication variations (see text for details). The marker shows peak fidelity for a given realization, error bar indicates the $F_R > 0.9$ bandwidth. The grey points show results obtained when $n_{g,a/b}$ and φ_{ext} are optimized for the ideal parameters listed in Fig. 3(c). Red points show fidelities obtained when $n_{g,a/b}$ and φ_{ext} are optimized for each realization. (b) upper panel: Peak fidelities as a function of photon frequency, for the chiral interface with parameters given in Fig. 3(c) and 100 samples of transmon Josephson energy E_{Jt} between $6 \sim 22$ hGHz. For each red dot thereof, the vertically aligned markers in the lower panel shows the adaptively optimized $n_{g,a/b}$ and φ_{ext} .

the $F_{R/L} > 0.9$ bandwidth (horizontal error bar). While the performance is generally good, certain instances with poor chiral fidelity are observed. Next, for each sample that has a maximal fidelity less than 0.99, we search for values of $n_{g,a/b}$ and φ_{ext} that improve the performance. The red points in Fig. 4(a) show the result of such optimization. We are always able to tune the maximal fidelity above 0.99. Additional details about how the maximal fidelity and bandwidth depend on $n_{g,a/b}$ and φ_{ext} are given in the Supplemental Material [39].

Additionally, flux-tunable transmons [27] enables tuning of the operating frequency of our device. We consider the parameters listed in Fig. 3(c) (including the separation d). For 100 values of E_{Jt} between $6 \sim 22$ hGHz, we optimize the peak fidelity to be higher than 0.99 by tuning $n_{g,a/b}$ and φ_{ext} . The results are presented in Fig. 4(b). It shows that for photons in a band of 3 GHz width, the same device can always be tuned to provide an excellent chiral interaction. This broad adaptability is rooted in the breaking of TRS. When we tune E_{Jt} , ω_{02} changes and so does the phase $k_0 d$ with $k_0 = \omega_{02}/v_g$. Adjusting the flux ϕ , however, allows us to achieve complete destructive interference in one of the directions. Our chiral interface thus works in principle as long as $k_0 d \neq 0 \pmod{\pi}$.

Discussion and conclusion. The bandwidth for $F_{R/L}(\omega) > 0.9$ is about 25 MHz in Fig. 3(a). This is limited by the transmon decay rate, which is typically

on the order of 100 MHz. The bandwidth can thus be directly enhanced by designing transmons with larger decay rates. We note however that as the decay rate approaches roughly a tenth of the transition frequency ($0.1\omega_0/2\pi \sim 500\text{MHz}$) the system reaches the ultra-strong coupling regime of waveguide QED [42] requiring a more advanced theoretical description [43, 44].

Our interface relies on the 2nd excited state. This raises the concern that decay to the 1st excited state may jeopardize the performance. This transition is negligible for two reasons. First, the transition matrix element is tiny (vanishing in our simplified model $\langle\Psi_-|\hat{n}_{A/B}|\Psi_{de}\rangle = 0$). Second, the waveguide mode density at $\omega_{12}/2\pi = (\omega_{02} - \omega_{01})/2\pi \sim 100\text{MHz}$ is low. As a result, the decay rate to the 1st excited state is numerically found to be $\gamma_{12}/2\pi \sim 10\text{kHz}$, which is much smaller than $\gamma_{02}/2\pi \sim 100\text{MHz}$. Similarly, the intrinsic loss of the components involved can be made well below 0.1MHz [34, 45]. This is much less than the decay rate to the waveguide and hence negligible [39].

In conclusion, we have shown that by introducing two transmons, a passive charge-noise insensitive chiral photonic interface can be build, based on a core consisting of CPBs and an external magnetic flux that breaks TRS. The interface has rich tunability, making it tolerant to experimentally relevant fabrication variations. The bandwidth of $F_{R/L} > 0.9$ is a few tens of MHz for realistic transmon parameters with decay rates typically around 100MHz. With tunable transmons (SQUIDS), our design can be tuned in a band as wide as a few GHz. The lateral dimension of the entire circulator can be a few millimeters [39]. These properties makes our chiral interface highly attractive for e.g., on chip routing of microwave signals [10, 14–23, 36, 37] as well as fundamental studies of chiral waveguide QED [3, 4, 7, 46].

A. S. Sørensen thanks Peter Lodahl, Per Delsing and Göran Johansson for useful discussions. M. Kjaergaard gratefully acknowledges helpful and insightful discussions with Bharath Kannan. Y.-X. Zhang and A. S. Sørensen thank Jacob M. Taylor and Brittany Richman for insightful discussions. Y.-X. Zhang, M. Kjaergaard & A. S. Sørensen acknowledge financial support from the Danish National Research Foundation. M. Kjaergaard was also supported by Villum Fonden (grant 37467) through a Villum Young Investigator grant.

* iyxz@nbi.ku.dk

- [1] C. W. Gardiner, *Phys. Rev. Lett.* **70**, 2269 (1993).
- [2] H. J. Carmichael, *Phys. Rev. Lett.* **70**, 2273 (1993).
- [3] T. Ramos, H. Pichler, A. J. Daley, and P. Zoller, *Phys. Rev. Lett.* **113**, 237203 (2014).
- [4] I. M. Mirza and J. C. Schotland, *Phys. Rev. A* **94**, 012302 (2016).
- [5] J.-T. Shen and S. Fan, *Phys. Rev. A* **76**, 062709 (2007).
- [6] H. Zheng, D. J. Gauthier, and H. U. Baranger, *Phys. Rev. Lett.* **107**, 223601 (2011).
- [7] S. Mahmoodian, G. Calajó, D. E. Chang, K. Hammerer, and A. S. Sørensen, *Phys. Rev. X* **10**, 031011 (2020).
- [8] V. I. Yudson, *Zh. Eksp. Teor. Fiz.* **88**, 1757 (1985).
- [9] P. Lodahl, S. Mahmoodian, S. Stobbe, A. Rauschenbeutel, P. Schneeweiss, J. Volz, H. Pichler, and P. Zoller, *Nature* **541**, 473 (2017).
- [10] I.-C. Hoi, C. M. Wilson, G. Johansson, T. Palomaki, B. Peropadre, and P. Delsing, *Phys. Rev. Lett.* **107**, 073601 (2011).
- [11] A. Blais, A. L. Grimsmo, S. Girvin, and A. Wallraff, *Reviews of Modern Physics* **93** (2021), 10.1103/revmodphys.93.025005.
- [12] D. Roy, C. M. Wilson, and O. Firstenberg, *Rev. Mod. Phys.* **89**, 021001 (2017).
- [13] C. Caloz, A. Alù, S. Tretyakov, D. Sounas, K. Achouri, and Z.-L. Deck-Léger, *Phys. Rev. Applied* **10**, 047001 (2018).
- [14] K. M. Sliwa, M. Hatridge, A. Narla, S. Shankar, L. Frunzio, R. J. Schoelkopf, and M. H. Devoret, *Phys. Rev. X* **5**, 041020 (2015).
- [15] B. Abdo, K. Sliwa, S. Shankar, M. Hatridge, L. Frunzio, R. Schoelkopf, and M. Devoret, *Phys. Rev. Lett.* **112**, 167701 (2014).
- [16] B. Abdo, N. T. Bronn, O. Jinka, S. Olivadese, A. D. Córcoles, V. P. Adiga, M. Brink, R. E. Lake, X. Wu, D. P. Pappas, and J. M. Chow, *Nature Communications* **10**, 3154 (2019).
- [17] J. Kerckhoff, K. Lalumière, B. J. Chapman, A. Blais, and K. W. Lehnert, *Phys. Rev. Applied* **4**, 034002 (2015).
- [18] S. Barzanjeh, M. Wulf, M. Peruzzo, M. Kalaei, P. B. Dieterle, O. Painter, and J. M. Fink, *Nature Communications* **8** (2017), 10.1038/s41467-017-01304-x.
- [19] A. Metelmann and H. E. Türeci, *Phys. Rev. A* **97**, 043833 (2018).
- [20] A. Kamal, J. Clarke, and M. H. Devoret, *Nature Physics* **7**, 311 (2011).
- [21] N. A. Estep, D. L. Sounas, J. Soric, and A. Alù, *Nature Physics* **10**, 923 (2014).
- [22] P. Roushan, C. Neill, A. Megrant, Y. Chen, R. Babush, R. Barends, B. Campbell, Z. Chen, B. Chiaro, A. Dunsworth, A. Fowler, E. Jeffrey, J. Kelly, E. Lucero, J. Mutus, P. J. J. O’Malley, M. Neeley, C. Quintana, D. Sank, A. Vainsencher, J. Wenner, T. White, E. Kapit, H. Neven, and J. Martinis, *Nature Physics* **13**, 146 (2016).
- [23] B. J. Chapman, E. I. Rosenthal, and K. W. Lehnert, *Phys. Rev. Applied* **11**, 044048 (2019).
- [24] J. Koch, A. A. Houck, K. L. Hur, and S. M. Girvin, *Physical Review A* **82** (2010), 10.1103/physreva.82.043811.
- [25] A. Wallraff, D. I. Schuster, A. Blais, L. Frunzio, R.-S. Huang, J. Majer, S. Kumar, S. M. Girvin, and R. J. Schoelkopf, *Nature* **431**, 162 (2004).
- [26] C. Müller, S. Guan, N. Vogt, J. H. Cole, and T. M. Stace, *Phys. Rev. Lett.* **120**, 213602 (2018).
- [27] J. Koch, T. M. Yu, J. Gambetta, A. A. Houck, D. I. Schuster, J. Majer, A. Blais, M. H. Devoret, S. M. Girvin, and R. J. Schoelkopf, *Phys. Rev. A* **76**, 042319 (2007).
- [28] C. R. i Carceller, *Chiral photon interaction mediated by a superconducting circuit QED*, Master’s thesis, University of Copenhagen (2020).
- [29] B. Richman and J. M. Taylor, *PRX Quantum* **2**, 030309 (2021).

- [30] A. Frisk Kockum, P. Delsing, and G. Johansson, *Phys. Rev. A* **90**, 013837 (2014).
- [31] A. F. Kockum, in *International Symposium on Mathematics, Quantum Theory, and Cryptography*, edited by T. Takagi, M. Wakayama, K. Tanaka, N. Kunihiro, K. Kimoto, and Y. Ikematsu (Springer Singapore, 2021).
- [32] B. Kannan, M. J. Ruckriegel, D. L. Campbell, A. F. Kockum, J. Braumüller, D. K. Kim, M. Kjaergaard, P. Krantz, A. Melville, B. M. Niedzielski, A. Vepsäläinen, R. Winik, J. L. Yoder, F. Nori, T. P. Orlando, S. Gustavsson, and W. D. Oliver, *Nature* **583**, 775 (2020).
- [33] E. Arimondo and G. Orriols, *Lettere Al Nuovo Cimento Series 2* **17**, 333 (1976).
- [34] A. P. M. Place, L. V. H. Rodgers, P. Mundada, B. M. Smitham, M. Fitzpatrick, Z. Leng, A. Premkumar, J. Bryon, A. Vrajitoarea, S. Sussman, G. Cheng, T. Madhavan, H. K. Babla, X. H. Le, Y. Gang, B. Jäck, A. Gye-nis, N. Yao, R. J. Cava, N. P. de Leon, and A. A. Houck, *Nature Communications* **12** (2021), 10.1038/s41467-021-22030-5.
- [35] M. Kjaergaard, M. E. Schwartz, J. Braumüller, P. Krantz, J. I.-J. Wang, S. Gustavsson, and W. D. Oliver, *Annual Review of Condensed Matter Physics* **11**, 369 (2020).
- [36] P.-O. Guimond, B. Vermersch, M. L. Juan, A. Sharafiev, G. Kirchmair, and P. Zoller, *npj Quantum Information* **6** (2020), 10.1038/s41534-020-0261-9.
- [37] N. Gheeraert, S. Kono, and Y. Nakamura, *Phys. Rev. A* **102**, 053720 (2020).
- [38] X. Wang and H. rong Li, “Chiral quantum network with giant atoms,” (2021), [arXiv:2106.13187 \[quant-ph\]](https://arxiv.org/abs/2106.13187).
- [39] *See Supplemental Material for detailed derivations and additional plots.*
- [40] D. Vion, *Science* **296**, 886 (2002).
- [41] M. Mirhosseini, E. Kim, X. Zhang, A. Sipahigil, P. B. Dieterle, A. J. Keller, A. Asenjo-Garcia, D. E. Chang, and O. Painter, *Nature* **569**, 692 (2019).
- [42] P. Forn-Díaz, J. J. García-Ripoll, B. Peropadre, J.-L. Orgiazzi, M. A. Yurtalan, R. Belyansky, C. M. Wilson, and A. Lupascu, *Nature Physics* **13**, 39 (2016).
- [43] E. Sanchez-Burillo, D. Zueco, J. J. Garcia-Ripoll, and L. Martin-Moreno, *Phys. Rev. Lett.* **113**, 263604 (2014).
- [44] T. Shi, Y. Chang, and J. J. García-Ripoll, *Phys. Rev. Lett.* **120**, 153602 (2018).
- [45] R. Barends, J. Kelly, A. Megrant, D. Sank, E. Jeffrey, Y. Chen, Y. Yin, B. Chiaro, J. Mutus, C. Neill, P. O’Malley, P. Roushan, J. Wenner, T. C. White, A. N. Cleland, and J. M. Martinis, *Phys. Rev. Lett.* **111**, 080502 (2013).
- [46] S. Mahmoodian, M. Čepulkovskis, S. Das, P. Lodahl, K. Hammerer, and A. S. Sørensen, *Phys. Rev. Lett.* **121**, 143601 (2018).

Supplemental Material for “A Charge-Noise Insensitive Chiral Photonic Interface for Waveguide Circuit QED”

Yu-Xiang Zhang,¹ Carles R. i Carceller,² Morten Kjaergaard,³ and Anders S. Sørensen¹

¹*Center for Hybrid Quantum Networks (Hy-Q), The Niels Bohr Institute, University of Copenhagen, Blegdamsvej 17, 2100 Copenhagen Ø, Denmark*

²*Department of Physics, Technical University of Denmark, Fysikvej 307, 2800 Kgs. Lyngby, Denmark*

³*Center for Quantum Devices, Niels Bohr Institute, University of Copenhagen, 2100 Copenhagen Ø, Denmark*

(Dated: December 2, 2021)

This Supplemental Material is organized as follows: In Sec. **S-I**, we derive the Hamiltonians of the chiral interface and the coupling to the transmission line waveguide, and present the Hilbert space truncation used in all the numerical calculations. In Sec. **S-II**, we discuss the equivalence between our bi-CPB core and the Josephson junction ring proposed in Ref. [S1]. In Sec. **S-III**, we derive the single-photon scattering matrix of the chiral interface using the standard input-output formalism. In Sec. **S-IV**, we show data parallel to that presented in the main text, but for a different family of device parameters. In Sec. **S-V**, we calculate the maximal fidelity and bandwidth of $F_{R/L} > 0.9$ for different values of the CPB offset charges $n_{g,a(b)}$ and constant external flux φ_{ext} , in order to demonstrate that tuning $n_{g,a(b)}$ and φ_{ext} is able to circumvent fabrication variation. In Sec. **S-VI** we estimate the geometric size of the whole device, and the influence of inherent decay of the device to the fidelity of chirality.

S-I. THEORETICAL FORMALISM FOR THE CHIRAL INTERFACE

In this section, we introduce the Hamiltonian of the chiral interface, including the artificial atoms and the transmission line waveguide. This section is organized as follows: In Sec. **S-IS-I.A** we present a discrete model for the transmission line, which can be conveniently integrated into the waveguide-“giant atom” coupling. In Sec. **S-IS-I.B** we elaborate on the Hamiltonian of the artificial giant atom. In Sec. **S-IS-I.C** we present the way we numerically diagonalize the Hamiltonian of the artificial atom.

S-I.A. Quantization of the Transmission Line Waveguide

We assume that the transmission line is infinite. In the literature, the one-dimensional continuum of waveguide modes are usually described through a continuous flux field $\phi(x)$. The Lagrangian of the waveguide reads

$$L_{tr} = \int_{-\infty}^{\infty} dx \left[\frac{1}{2} c \dot{\phi}^2 - \frac{1}{2l} (\partial_x \phi)^2 \right]. \quad (\text{S1})$$

where c and l are the capacitance and inductance per unit length.

For our purpose it is convenient to describe the waveguide as a discrete series of coupled LC-oscillators. In this model each oscillator has capacitance $c\delta_z$ and inductance $l\delta_z$ with δ_z an infinitesimal unit length. The coupling capacitor has finite physical length, as illustrated in Fig. **S1**. Since the coupling cannot distinguish modes with wavelengths shorter than this length, it is convenient to define δ_z to be this length, so that the variable relevant to the

coupling is

$$\bar{\phi}(x_{l/r}) = \frac{1}{\delta_z} \int_{x_{l/r}-\delta_z/2}^{x_{l/r}+\delta_z/2} dx \phi(x). \quad (\text{S2})$$

We then obtain a discrete model:

$$L_{tr} = \sum_{n=-\infty}^{+\infty} \left[\frac{1}{2} c \delta_z \dot{\phi}_n^2 - \frac{1}{2l \delta_z} (\phi_{n+1} - \phi_n)^2 \right] \quad (\text{S3})$$

The corresponding Hamiltonian is given by

$$H_{tr} = \sum_{n=-\infty}^{\infty} \left[\frac{1}{2c\delta_z} q_n^2 + \frac{1}{2l\delta_z} (\phi_{n+1} - \phi_n)^2 \right]. \quad (\text{S4})$$

To diagonalize the Hamiltonian, we move to momentum representation:

$$\begin{aligned} \phi_m &= \int_{-\pi}^{\pi} \frac{dk}{2\pi} \phi_k e^{imk} \\ q_m &= \int_{-\pi}^{\pi} \frac{dk}{2\pi} q_k e^{-imk}, \end{aligned} \quad (\text{S5})$$

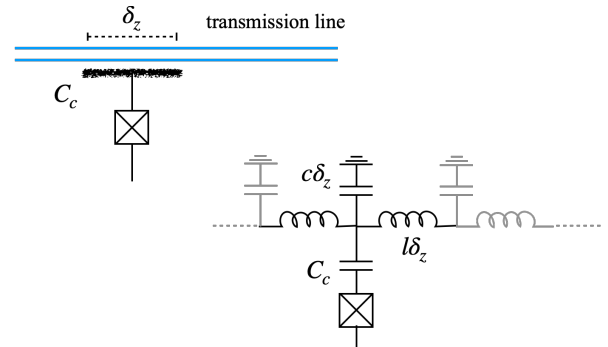


Figure S1. Capacitive coupling to the transmission line. Upper panel: continuous model; Lower panel: discrete model.

Since $[\phi_m, q_n] = i\hbar\delta_{mn}$, we have $[\phi_k, q_{k'}] = i\hbar 2\pi\delta(k - k')$. Note that k is here defined to be dimensionless. Substituting the above equations into Eq. (S4) and using the equality $\sum_{n=-\infty}^{\infty} e^{-ikn} = 2\pi\delta(k)$, we get

$$H_{tr} = \frac{1}{2} \int_{-\pi}^{\pi} \frac{dk}{2\pi} \left(\frac{q_k q_{-k}}{c\delta_z} + 4 \left| \sin \frac{k}{2} \right|^2 \frac{\phi_k \phi_{-k}}{l\delta_z} \right). \quad (\text{S6})$$

Next, we introduce bosonic ladder operators b_k and b_k^\dagger satisfying $[b_k, b_{k'}^\dagger] = 2\pi\delta(k - k')$, and

$$\phi_k = \sqrt{\frac{\hbar Z_0}{4|\sin(k/2)|}} (b_k + b_{-k}^\dagger), \quad (\text{S7a})$$

$$q_k = i \sqrt{\frac{\hbar |\sin(k/2)|}{Z_0}} (b_k^\dagger - b_{-k}), \quad (\text{S7b})$$

where $Z_0 = \sqrt{l/c}$ is the impedance. Then the Hamiltonian is diagonalized to $H_{tr} = \int_{-\pi}^{\pi} \frac{dk}{2\pi} \hbar\omega_k b_k^\dagger b_k$ with

$$\omega_k = \frac{2}{\sqrt{lc}\delta_z} |\sin(k/2)|. \quad (\text{S8})$$

The phase and charge are expressed as

$$\phi_m = \frac{1}{2} \int_{-\pi}^{\pi} \frac{dk}{2\pi} \frac{\sqrt{\hbar Z_0}}{\sqrt{|\sin(k/2)|}} (e^{ikx_m} b_k + e^{-ikx_m} b_k^\dagger), \quad (\text{S9a})$$

$$q_m = i \int_{-\pi}^{\pi} \frac{dk}{2\pi} \sqrt{\frac{\hbar}{Z_0}} \left| \sin \frac{k}{2} \right| (e^{-ikx_m} b_k^\dagger - e^{ikx_m} b_k). \quad (\text{S9b})$$

The two unit cells connected to the ‘‘giant atom’’ will be denoted by ‘‘l’’ and ‘‘r’’. Their charge number operators $\hat{n}_{l/r}$ are obtained from the charge operators $\hat{q}_{a/b}$ via the relation $\hat{q}_{l/r} = 2e\hat{n}_{l/r}$.

S-I.B. Hamiltonian of the Chiral Interface

At first, we consider a cluster composed by the two transmons, the bi-CPB core, and two sections of the transmission line, x_l and x_r . The Hamiltonian for these parts reads

$$H_0 = 2e^2 \hat{\mathbf{n}} \mathbf{C}^{-1} \hat{\mathbf{n}} - \sum_{i=a,b} E_{J,i} \cos(\hat{\varphi}_i) - \sum_{j=A,B} E_{Jt,j} \cos(\hat{\varphi}_j) - E_{J,ab} \cos(\hat{\varphi}_a - \hat{\varphi}_b - \varphi_{\text{ext}}) + \frac{1}{2l\delta_z} (\hat{\phi}_l^2 + \hat{\phi}_r^2), \quad (\text{S10})$$

where $\hat{\mathbf{n}} = (\hat{n}_l, \hat{n}_A, \hat{n}_a - n_{g,a}, \hat{n}_r, \hat{n}_B, \hat{n}_b - n_{g,b})^\top$. The dimensionless flux used in the Josephson potentials is defined in the form of $\hat{\varphi} = \hat{\phi} \times 2\pi/\Phi_0$, and the capacitance

matrix is given by

$$\mathbf{C} = \begin{pmatrix} c\delta_z & -C_{c,A} & 0 & 0 & 0 & 0 \\ -C_{c,A} & C_{\Sigma,A} & -C_{q,a} & 0 & 0 & 0 \\ 0 & -C_{q,a} & C_{\Sigma,a} & 0 & 0 & -C_{ab} \\ 0 & 0 & 0 & c\delta_z & -C_{c,B} & 0 \\ 0 & 0 & 0 & -C_{c,B} & C_{\Sigma,B} & -C_{q,b} \\ 0 & 0 & -C_{ab} & 0 & -C_{q,b} & C_{\Sigma,b} \end{pmatrix} \quad (\text{S11})$$

where $C_{\Sigma,A/B} = C_{c,A/B} + C_{t,A/B} + C_{q,a/b}$ is the total capacitance of transmon-A/B, and $C_{\Sigma,a/b} = C_{\Sigma,a/b} + C_{q,a/b} + C_{ab}$ is the total capacitance of CPB-a/b. Note that offset charges of the transmons are not included. This is justified because for the low energy excitations, the influence of offset charges is exponentially suppressed if E_{Jt} is much larger than the transmon charging energy [S2].

H_0 can be decomposed into the ‘‘system’’ that consists of transmon-A/B and the bi-CPB core:

$$H_{sys} = 2e^2 \sum_{i,i'=a,b} \mathbf{C}_{i,i'}^{-1} (\hat{n}_i - n_{g,i})(\hat{n}_{i'} - n_{g,i'}) - \sum_{i=a,b} E_{J,i} \cos(\hat{\varphi}_i) - E_{J,ab} \cos(\hat{\varphi}_a - \hat{\varphi}_b - \varphi_{\text{ext}}) + 2e^2 \sum_{j,j'=A,B} \mathbf{C}_{j,j'}^{-1} \hat{n}_j \hat{n}_{j'} - \sum_{j=A,B} E_{Jt,j} \cos(\hat{\varphi}_j) + 4e^2 \sum_{i=a,b} \sum_{j=A,B} \mathbf{C}_{ij}^{-1} \hat{n}_j (\hat{n}_i - n_{g,i}), \quad (\text{S12})$$

where terms in the last line covers Eq. (3) of the main text. The interactions to the two unit cells ‘‘l’’ and ‘‘r’’ of the transmission line:

$$H_{int} = 4e^2 \sum_{\xi=l,r} \sum_{i=a,b} \mathbf{C}_{\xi,i}^{-1} \hat{n}_\xi (\hat{n}_i - n_{g,i}) + 4e^2 \sum_{\xi=l,r} \sum_{j=A,B} \mathbf{C}_{\xi,j}^{-1} \hat{n}_\xi \hat{n}_j. \quad (\text{S13})$$

We neglect the corrections to the charging energy from the two transmission line unit cells, and also neglect their direct interaction (expressed by terms with coefficient $C_{l,r}^{-1}$), which is bridged by the coupled core and transmon system. This means that the transmission line Hamiltonian is H_{tr} (S4) without corrections other than from the coupling to the excitations of the systems. That is, the total Hamiltonian is written as

$$H = H_{sys} + H_{tr} + H_{int}. \quad (\text{S14})$$

S-I.C. Hilbert Space Truncation Used in the Numerical Calculations

We numerically diagonalize H_{sys} (S12) in a truncated Hilbert space

$$\mathcal{H} = \mathcal{H}_A \otimes \mathcal{H}_B \otimes \mathcal{H}_a \otimes \mathcal{H}_b. \quad (\text{S15})$$

Dev-1: main text Fig. 3(c)					
$\mathcal{H}_t/\mathcal{H}_{\text{CPB}}$	ω_{01}	ω_{02}	ω_{03}	ω_{04}	ω_{05}
$3^2/10^2$	5.3321	5.6583	6.1254	9.4978	10.8150
$4^2/8^2$	5.3292	5.6640	6.1222	9.4998	10.7921
$4^2/10^2$	5.3292	5.6640	6.1222	9.4998	10.7921
$5^2/12^2$	5.3294	5.6636	6.1224	9.4997	10.7941
Dev-2: Fig. S3(d)					
$\mathcal{H}_t/\mathcal{H}_{\text{CPB}}$	ω_{01}	ω_{02}	ω_{03}	ω_{04}	ω_{05}
$3^2/10^2$	4.8741	5.2474	5.6737	9.1045	9.9481
$4^2/8^2$	4.8744	5.2463	5.6742	9.1033	9.9654
$4^2/10^2$	4.8744	5.2463	5.6742	9.1033	9.9654
$5^2/12^2$	4.8745	5.2462	5.6743	9.1033	9.9621

Table I. Energy levels of the chiral interface (in units of $h\text{GHz}$) calculated with different truncations of the Hilbert space. The column $\mathcal{H}_t/\mathcal{H}_{\text{CPB}}$ lists the dimensions of the Hilbert spaces of the transmons and the bi-CPB core.

Therein, \mathcal{H}_A is spanned by the lower energy eigenstates of the bare transmon Hamiltonian:

$$H_A = 2e^2 C_{A,A}^{-1} \hat{n}_A^2 - E_{J,t} \cos(\hat{\varphi}_A) \quad (\text{S16})$$

and similarly for \mathcal{H}_B . The CPB Hilbert space $\mathcal{H}_{a/b}$ is spanned by the charge number states, i.e., the eigenstates of $\hat{n}_{a/b}$ with eigenvalue $n = -3, -2, \dots, 4$ (the ‘‘sweet spot’’ satisfying $0.5 < n_{g,a/b} < 1$ is chosen). The dimensions of each space is varied to ensure the convergence of the eigenvalues of the ground and low-excitation eigenvalues. As shown in Tab. I, we find that it is sufficient to take

$$\dim \mathcal{H}_{A/B} = 4, \dim \mathcal{H}_{a/b} = 8. \quad (\text{S17})$$

That is, the numerical diagonalization is implemented in a 1024-dimensional Hilbert space. After the diagonalization, we neglect most of the eigenstates and keep only the lowest four excited states. These states are then substituted into the general formula for the scattering matrix, to be introduced later, to calculate the fidelity of the circulator.

S-II. EQUIVALENCE BETWEEN THE BI-CPB CORE AND THE JOSEPHSON JUNCTION RING

In Fig. S2 we illustrated the 3-port Josephson ring of Ref. [S1] and the bi-CPB core used in the main text. Here we show the equivalence between them.

We derive the Hamiltonian of the Josephson ring following Ref. [S1]. The total charge of the three CPBs, $\hat{N} = \hat{n}_a + \hat{n}_b + \hat{n}_c$, is conserved. Thus, we restrict the description to the subspace spanned by states $|\psi\rangle$ satisfying $\langle \psi | \hat{N} | \psi \rangle = N_0$. In this subspace, we apply the following canonical transformations

$$\begin{aligned} \hat{\varphi}_a &= \hat{\varphi}'_a + \hat{\varphi}'_c, \hat{\varphi}_b = \hat{\varphi}'_c - \hat{\varphi}'_b, \hat{\varphi}_c = \hat{\varphi}'_c, \\ \hat{n}_a &= \hat{n}'_a, \hat{n}_b = -\hat{n}'_b, \hat{n}_c = -\hat{n}'_a + \hat{n}'_b + \hat{n}'_c, \end{aligned} \quad (\text{S18})$$

where $\hat{n}'_c = \hat{N}$ is conserved hence the conjugate variable $\hat{\varphi}'_c$ is cyclic. Therefore, the Hamiltonian restricted to this subspace has the form

$$\begin{aligned} H_{(N_0)} &= 4E_C \left[(\hat{n}'_a - n'_{g,a})^2 + (\hat{n}'_b + n'_{g,b})^2 - \hat{n}'_a \hat{n}'_b \right] \\ &\quad - E_J \cos(\hat{\varphi}'_a - \frac{\varphi_{\text{ext}}}{3}) - E_J \cos(\hat{\varphi}'_b - \frac{\varphi_{\text{ext}}}{3}) \\ &\quad - E_J \cos(\hat{\varphi}'_a + \hat{\varphi}'_b + \frac{\varphi_{\text{ext}}}{3}) \end{aligned} \quad (\text{S19})$$

where the junctions are assumed to be identical for convenience, $n'_{g,a} = \frac{1}{2}(n_{g,a} - n_{g,c} + N_0)$ and $n'_{g,b} = \frac{1}{2}(n_{g,b} - n_{g,c} + N_0)$.

Next, we perform the transformations $\hat{\varphi}'_{a/b} \rightarrow \hat{\varphi}'_{a/b} + \frac{1}{3}\varphi_{\text{ext}}$, which is then followed by

$$\hat{\varphi}'_b \rightarrow -\hat{\varphi}'_b, \hat{n}'_b \rightarrow -\hat{n}'_b. \quad (\text{S20})$$

With this replacement, the Hamiltonian is brought into the form

$$\begin{aligned} H_{(N_0)} &= 4E_C \left[(\hat{n}'_a - n'_{g,a})^2 + (\hat{n}'_b - n'_{g,b})^2 + \hat{n}'_a \hat{n}'_b \right] \\ &\quad - E_J \cos(\hat{\varphi}'_a) - E_J \cos(\hat{\varphi}'_b) \\ &\quad - E_J \cos(\hat{\varphi}'_a - \hat{\varphi}'_b + \varphi_{\text{ext}}). \end{aligned} \quad (\text{S21})$$

This is formally equivalent to the Hamiltonian of our bi-CPB with for suitable charging energies and offset charges $\tilde{n}_{g,a/b}$ given by

$$\begin{aligned} \tilde{n}_{g,a} &= \frac{4}{3}n'_{g,a} - \frac{2}{3}n'_{g,b}, \\ \tilde{n}_{g,b} &= \frac{4}{3}n'_{g,b} - \frac{2}{3}n'_{g,a}. \end{aligned} \quad (\text{S22})$$

S-III. SINGLE PHOTON SCATTERING MATRIX

Here we derive the scattering matrix for a single incident photon. The formulas derived below will be used to calculate the fidelity of a circulator based on the chiral interfaces with and without the transmons. It will be convenient to expand the operators of the chiral system on eigenstates of its Hamiltonian, which can then be

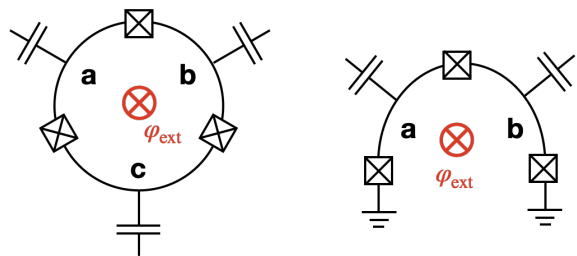


Figure S2. Left panel: 3-port Josephson junction ring; Right panel: 2-port bi-CPB core.

specified on demand. We will apply the rotating-wave approximation to the interaction between the chiral system and the transmission line waveguide (S13). This means that an operator representing the emission of a photon is always associated with a jump from states of higher energy to lower, and vice versa. For simplicity, we also omit the inelastic scattering where a single input photon is scattered into two or more photons of lower frequency. Thus, we consider only the decay from an excited state to the ground state excluding intermediate lower excited

state. This is justified in the discussion section of the main text. In the treatment below we include the Lamb shift caused by coupling to the waveguide but neglect e.g. effects caused by divergences of the high frequency light modes and corrections to the dipole approximation of the transmon-waveguide coupling. Such effect should be absorbed into the model presented below by renormalizing parameters like energy levels and coupling strengths. A more sophisticated theory which carefully addresses all these effects is beyond of the scope of this work.

Explicitly, the system Hamiltonian is expressed as

$$H/\hbar = \int_{-\pi}^{\pi} \frac{dk}{2\pi} \omega_k b_k^\dagger b_k + \sum_n e_n |\phi_n\rangle \langle \phi_n| + i \sum_{\xi, i; n} \int_{-\pi}^{\pi} \frac{dk}{2\pi} \sqrt{\kappa_{\xi ik}} b_k^\dagger e^{-ikx_\xi} \eta_{in} \sigma_n^- + h.c. \quad (\text{S23})$$

where index $\xi \in \{l, r\}$, index n runs over the numerically obtained excited states $|\phi_n\rangle$ of H_{sys} ($n \leq 4$ in our calculation), index $i \in \{a, b, A, B\}$, $\sigma_n^- = |g\rangle \langle \phi_n|$ and $\eta_{in} \equiv \langle g | \hat{n}_i | \phi_n \rangle$ with $|g\rangle$ the ground state of H_{sys} . Decay between the excited states are neglected, as explained above. The coupling strength is

$$\sqrt{\kappa_{\xi ik}} = 2eC_{\xi, i}^{-1} \sqrt{\frac{|\sin(k/2)|}{\hbar Z_0}}. \quad (\text{S24})$$

To describe a situation where a single photon is incident, we consider the single-excitation ansatz

$$|\Psi\rangle = \sum_n c_n |\phi_n\rangle + \int_{-\pi}^{\pi} \frac{dk}{2\pi} f_k b_k^\dagger |g, \emptyset\rangle, \quad (\text{S25})$$

where $|\emptyset\rangle$ is the vacuum of the waveguide photon. Then the Schrödinger equation leads to

$$i\partial_t c_n = c_n e_n - i \int_{-\pi}^{\pi} \frac{dk}{2\pi} f_k \sum_{\xi, i} e^{ikx_\xi} \sqrt{\kappa_{\xi ik}} \eta_{in}^*, \quad (\text{S26a})$$

$$i\partial_t f_k = \omega_k f_k + i \sum_{\xi, i, n} c_n e^{-ikx_\xi} \sqrt{\kappa_{\xi ik}} \eta_{in}. \quad (\text{S26b})$$

The second equation is formally solved in two ways

$$f_k(t) = f_k(t_0) e^{-i\omega_k(t-t_0)} + \sum_{\xi, i, n} e^{-ikx_\xi} \sqrt{\kappa_{\xi ik}} \eta_{in} \int_{t_0}^t d\tau e^{-i\omega_k(t-\tau)} c_n(\tau), \quad (\text{S27a})$$

and

$$f_k(t) = f_k(t_f) e^{-i\omega_k(t-t_f)} + \sum_{\xi, i, n} e^{-ikx_\xi} \sqrt{\kappa_{\xi ik}} \eta_{in} \int_{t_f}^t d\tau e^{-i\omega_k(t-\tau)} c_n(\tau). \quad (\text{S27b})$$

Therein, the input and output fields are defined as $f_k^{in}(t) = f_k(t_0) e^{-i\omega_k(t-t_0)}$ and $f_k^{out}(t) = f_k(t_f) e^{i\omega_k(t_f-t)}$, respectively. In Fourier space (assuming $t_f - t_0 = \infty$) we then obtain the input-output relation

$$F_k^{out}(\omega) - F_k^{in}(\omega) = 2\pi\delta(\omega - \omega_k) \sum_{\xi, i, n} e^{-ikx_\xi} \sqrt{\kappa_{\xi ik}} \eta_{in} C_n(\omega). \quad (\text{S28})$$

We substitute the input field solution Eq. (S27a) into Eq. (S26a) and obtain

$$(i\partial_t - e_n) c_n = -i \int_{-\pi}^{\pi} \frac{dk}{2\pi} \sum_{\xi, i} e^{ikx_\xi} \sqrt{\kappa_{\xi ik}} \eta_{in}^* f_k^{in}(t) - i \sum_{\xi\xi' ii' n'} \int_{-\pi}^{\pi} \frac{dk}{2\pi} e^{ik(x_\xi - x_{\xi'})} \sqrt{\kappa_{\xi ik} \kappa_{\xi' i' k}} \eta_{in}^* \eta_{i'n'} \int_{t_0}^t d\tau e^{-i\omega_k(t-\tau)} c_{n'}(\tau). \quad (\text{S29})$$

The integral of τ is evaluated as (assuming $t - t_0 \rightarrow \infty$)

$$\int_{t_0}^t d\tau e^{-i(\omega_k - \omega_0)(t - \tau)} \tilde{c}_{n'}(\tau) e^{-i\omega_0(t - t_0)} \approx c_{n'}(t) \frac{i}{\omega_0 - \omega_k + i0^+}. \quad (\text{S30})$$

The fast evolution part of $c_{n'}(t)$ is determined by the input frequency ω_0 . The term $\sqrt{\kappa_{\xi ik} \kappa_{\xi' i' k}}$ contributes a factor of $|\sin(k/2)|$. Then the integral over $k > 0$ is approximated by defining $q = k - k_0$ and extending the range of integral over q to infinity

$$e^{ik_0(x_\xi - x_{\xi'})} \left| \sin \frac{k_0}{2} \right| \int_{-\infty}^{\infty} \frac{dq}{2\pi} e^{iq(x_\xi - x_{\xi'})} \left(\mathcal{P} \frac{-i}{v_g q} + \pi \delta(v_g q) \right). \quad (\text{S31})$$

For the principal integral, we substitute $e^{iq\Delta x} = \cos(q\Delta x) + i \sin(q\Delta x)$ and notice that terms of cosine vanish and those of sine can be solved by $\int_{-\infty}^{\infty} dx \frac{\sin x}{x} = \pi$. That is, the integral over q of Eq. (S31) vanishes if $x_\xi - x_{\xi'} < 0$, equals $\frac{1}{v_g}$ if $x_\xi - x_{\xi'} > 0$, and equals $\frac{1}{2v_g}$ if $x_\xi = x_{\xi'}$. As to the integral of $k < 0$, it is approximated by, defining $k = -k_0 + q$,

$$e^{-ik_0(x_\xi - x_{\xi'})} \left| \sin \frac{k_0}{2} \right| \int_{-\infty}^{\infty} \frac{dq}{2\pi} e^{iq(x_\xi - x_{\xi'})} \left(\mathcal{P} \frac{i}{v_g q} + \pi \delta(v_g q) \right). \quad (\text{S32})$$

Similarly, now it vanishes if $x_\xi - x_{\xi'} > 0$, equals $\frac{1}{v_g}$ if $x_\xi - x_{\xi'} < 0$, and equals $\frac{1}{2v_g}$ if $x_\xi = x_{\xi'}$. Then we take it into the integral over k and obtain

$$\int_{-\pi}^{\pi} \frac{dk}{2\pi} e^{ik(x_\xi - x_{\xi'})} \frac{i |\sin(k/2)|}{\omega_0 - \omega_k + i0^+} \approx v_g^{-1} \left| \sin \frac{k_0}{2} \right| e^{ik_0|x_\xi - x_{\xi'}|} \quad (\text{S33})$$

where $k_0 = \omega_0/v_g > 0$. It leads to

$$(i\partial_t - e_n)c_n = -i \int_{-\pi}^{\pi} \frac{dk}{2\pi} \sum_{\xi, i} e^{ikx_\xi} \sqrt{\kappa_{\xi ik} \eta_{in}^*} f_k^{in}(t) - i \sum_{\xi', i', n'} \frac{\sqrt{\kappa_{\xi ik_0} \kappa_{\xi' i' k_0}}}{v_g} \eta_{in}^* \eta_{i'n'} e^{ik_0|x_\xi - x_{\xi'}|} c_{n'}. \quad (\text{S34})$$

In the Fourier space, it is expressed as

$$C_n(\omega) = -i \int_{-\pi}^{\pi} \frac{dk}{2\pi} \left[\omega \mathbb{I} - \hat{E} + i\Sigma \right]_{nm}^{-1} \alpha_m(k) F_k^{in}(\omega) \quad (\text{S35})$$

where $\hat{E}_{nm} = e_n \delta_{n,m}$ and

$$\alpha_m(k) = \sum_{\xi, i} e^{ikx_\xi} \sqrt{\kappa_{\xi ik} \eta_{im}^*} \quad (\text{S36a})$$

$$\Sigma_{n,m} = \frac{1}{v_g} \sum_{\xi, \xi', i, i'} \sqrt{\kappa_{\xi ik_0} \kappa_{\xi' i' k_0}} e^{ik_0|x_\xi - x_{\xi'}|} \eta_{in}^* \eta_{i'm}. \quad (\text{S36b})$$

Substituting it into Eq. (S28), we get

$$F_{k_0}^{out} - F_{k_0}^{in} = -i \frac{1}{v_g} \sum_{m,n} \alpha_n^*(k_0) \left[\omega_{k_0} \mathbb{I} - \hat{E} + i\Sigma \right]_{nm}^{-1} [\alpha_m(k_0) F_{k_0}^{in} + \alpha_m(-k_0) F_{-k_0}^{in}] \quad (\text{S37})$$

This leads to the scattering matrix

$$\begin{pmatrix} F_{k_0}^{out} \\ F_{-k_0}^{out} \end{pmatrix} = \begin{pmatrix} 1 - \frac{i}{v_g} \alpha_n^*(k_0) [(\omega_{k_0} - e_n) \mathbb{I} + i\Sigma]_{nm}^{-1} \alpha_m(k_0) & -\frac{i}{v_g} \alpha_n^*(k_0) [(\omega_{k_0} - e_n) \mathbb{I} + i\Sigma]_{nm}^{-1} \alpha_m(-k_0) \\ -\frac{i}{v_g} \alpha_n^*(-k_0) [(\omega_{k_0} - e_n) \mathbb{I} + i\Sigma]_{nm}^{-1} \alpha_m(k_0) & 1 - \frac{i}{v_g} \alpha_n^*(-k_0) [(\omega_{k_0} - e_n) \mathbb{I} + i\Sigma]_{nm}^{-1} \alpha_m(-k_0) \end{pmatrix} \begin{pmatrix} F_{k_0}^{in} \\ F_{-k_0}^{in} \end{pmatrix}. \quad (\text{S38})$$

In the evaluation of the scattering matrix, the coupling strengths are related to the physical parameters accord-

ing to the relation

$$\frac{\sqrt{\kappa_{\xi ik}\kappa_{\xi' i' k}}}{v_g} = (2ec\delta_z)^2 C_{\xi,i}^{-1} C_{\xi',i'}^{-1} \frac{1}{2\hbar} Z_0 \omega_k. \quad (\text{S39})$$

The fidelity of the circulator can be evaluated by substituting the matrix elements of Eq. (S38) into Eq. (2) of the main text.

S-IV. ADDITIONAL RESULTS FOR LEVEL STABILITY AND DEVICE TUNABILITY

In the main text, the numerical results are obtained for rather symmetric device parameters, that is, the capacitors used in the bi-CPB core are assumed to have identical capacitance, and $k_0 d$ and φ_{ext} are both taken to be 0.5π . To demonstrate that all these precise choices are not essential, we here present parallel calculations for another family of device parameters.

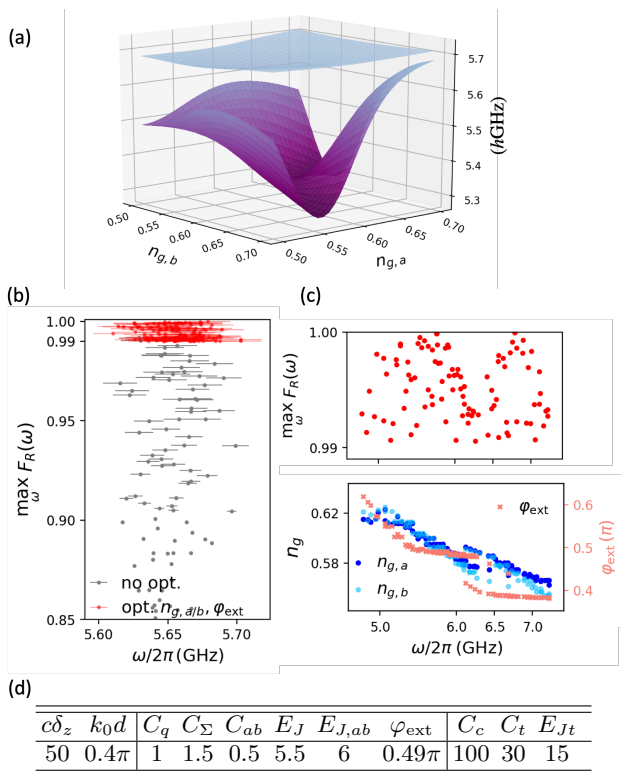


Figure S3. Results parallel to the main text but different device parameters. (a) The energy levels ω_{01} and ω_{02} as a function of offset charges $n_{g,a(b)}$. (b) 150 samplings of fabrication variations. (c) 100 examples of fidelity of chirality obtained by tuning transmon Josephson energies. (d) Device parameters. Units for the capacitances and the Josephson energies are fF and hGHz, respectively.

Results are plotted in Fig. S3 for the device parameters listed in Fig. S3(d). These plots are equivalent to those presented in the main text, and they convey the same message. Our optimization only aims at achiev-

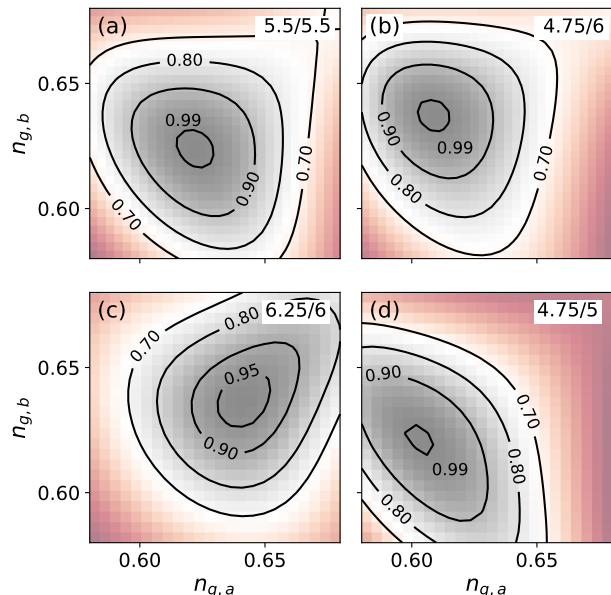


Figure S4. Maximal fidelity as a function of $n_{g,a}$ and $n_{g,b}$ for different values of $E_{J,a}/E_{J,b}$ labelled in the upper right corner of each sub-figure (in units of hGHz). The other device parameters are the same as in Fig. 3(c) of the main text.

ing $\max_{\omega} F_R(\omega) > 0.99$. Thus the adapted parameters shown in the lower panel of Fig. S3(c) are not unique.

S-V. DEPENDENCE OF FIDELITY AND BANDWIDTH ON THE CPB OFFSET CHARGES AND THE EXTERNAL FLUX

In the main text, we have shown that fabrication variations can be addressed by tuning the offset charges $n_{g,a/b}$ and the external flux φ_{ext} , but have not gone into details about the optimized values of them. Since the fabrication variations for capacitance ($\pm 1\%$) is smaller than that of Josephson energies ($\pm 10\%$), we focus on only the latter and elaborate on a few examples of extreme variations.

We use the device parameters listed in Fig. 3(c) of the main text, where $E_{J,ab} = 5$ hGHz and $E_{J,a} = E_{J,b} = 5.5$ hGHz. We consider three cases where $E_{J,a}/E_{J,b}$ deviate from the intended values significantly: one is smaller while the other is larger, both are larger, or both are smaller, than the intended values. The peak fidelity of the intended case and three examples of extreme fabrication variation are plotted in Fig. S4 as a function of $n_{g,a}$ and $n_{g,b}$, with φ_{ext} fixed at 0.5π . It shows that by adjusting only the offset charges, the fabrication variations of Fig. S4(b) and S4(d) can be addressed. In Fig. S4(c) the maximal fidelity cannot be lifted beyond 0.99. In this case, the external magnetic flux φ_{ext} must be tuned as well. We obtained $\max_{\omega} F_R = 0.996$ with parameters $n_{g,a} = 0.63$, $n_{g,b} = 0.631$ and $\varphi_{\text{ext}} = 0.534\pi$.

Next, we study how the bandwidth and peak fidelity depend on $n_{g,a/b}$ and φ_{ext} . For convenience, we assume

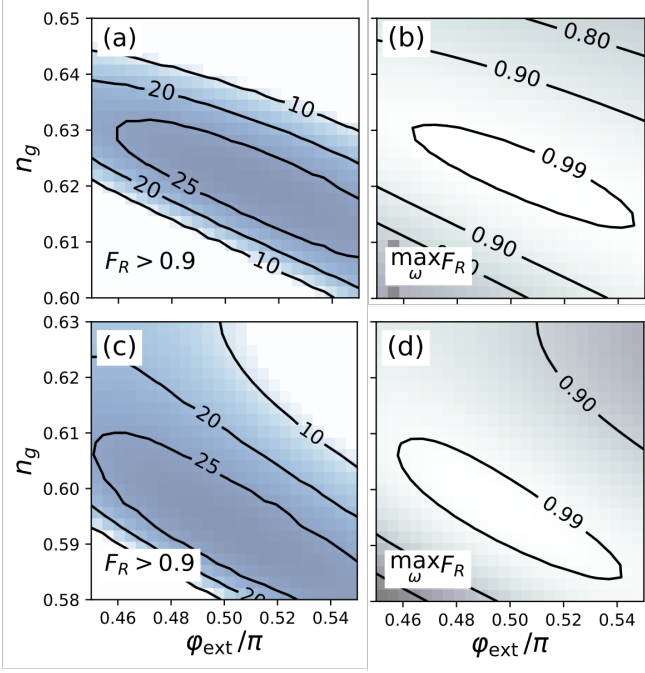


Figure S5. Dependence of the bandwidth for $F_R > 0.9$ (a,c, in units of MHz) and maximal fidelity $\max_{\omega} F_R(\omega)$ (b,d) on the offset charge and external flux. The device parameters are: (a,b) parameter listed in the main text Fig. 3(c); (c,d) parameter listed in Fig. S3(d).

$n_{g,a} = n_{g,b} = n_g$ and plot the results in Fig. S5 for the device parameters used in the main text, and those listed in Fig. S3(d). From Fig. S4 and S5 we can see that to stabilize the performance of the chiral interface, the offset charges $n_{g,a/b}$ and fluxes should be controlled at the percent level.

S-VI. GEOMETRIC SIZE AND INHERENT LOSS

Here we estimate the geometric size and inherent loss rate of the proposed photonic chiral interface. For typical

devices, the largest component of the system will most likely be the shunt capacitors of the transmons. The lateral length of these capacitors can be as large as $500\mu\text{m}$ in order to achieve a stronger coupling to the waveguide, such as the devices reported in Refs. [S3] and [S4]. (Recall that in the main text, we use a moderate assumption of $\delta_z = 250\mu\text{m}$). Meanwhile, the length of the transmission line between the two transmons is about a quarter of the resonant wavelength, which is roughly 1cm. The dimension of this can, however, be made much shorter by meandering the wire [S4]. The other components, Cooper-pair-boxes and flux rings of SQUIDs, are typically down to $10\mu\text{m} \times 10\mu\text{m}$ [S5, S6]. Therefore, the whole device might be placed in a square with side length being about a few millimeters. This demonstrates the on-chip compatibility of our proposal.

Taking the inherent loss at a rate γ_{in} into account, the highest fidelity of the chirality will be reduced by a small amount proportional to γ_{in}/γ_{02} . Although the Cooper-pair-boxes are sensitive to environmental charge noise, their excitations are strongly suppressed in our “dark state” configuration. In our device γ_{in} will thus mainly be determined by the transmons. Since T_1 of a transmon is typically $30 \sim 40\mu\text{s}$ [S7], we expect γ_{in}/γ_{02} to be well below 0.01, given that $\gamma_{02} \approx 50 \sim 100\text{MHz}$.

Next, we give a more precise evaluation of the performance of the chiral interface under the influence of inherent transmon loss at a rate γ_{in} . Following the approach of Ref. [S8], we take the transmon loss into account by the non-Hermitian Hamiltonian

$$H/\hbar = \int \frac{dk}{2\pi/d} v_g |k| b_k^\dagger b_k + (\omega_e - i\frac{\gamma_{in}}{2}) |\phi_e\rangle \langle \phi_e| + i\sqrt{\kappa} \int \frac{dk}{2\pi/d} \left(b_k (\sigma_A^\dagger + e^{ikd} \sigma_B^\dagger) - b_k^\dagger (\sigma_A + e^{-ikd} \sigma_B) \right), \quad (\text{S40})$$

where v_g is the waveguide group velocity. This non-Hermitian Hamiltonian describe the evolution of the system in the presence of decay and allows us to evaluate the probability for the photon to have the desired behavior through the norm of the wavefunction. Compared with Eq. (S23) the chiral interface is for simplicity represented by a single excited state $|\phi_e\rangle = \frac{1}{\sqrt{2}}(|1_A\rangle + e^{i\phi}|1_B\rangle)$ with eigen-energy ω_e . In our chiral photonic interface, ϕ can be controlled by the off-set charges $n_{g,a/b}$ and the external flux ϕ_{ext} , and ω_e is determined by the tunable transmon frequency. The transmon-waveguide coupling strength $\sqrt{\kappa}$ is related to the decay rate to the waveguide through $\Gamma = 2\kappa/v_g$.

The same derivations as Sec. S-III leads to the following formula for the scattering matrix:

$$\begin{pmatrix} F_{k_0}^{out} \\ F_{-k_0}^{out} \end{pmatrix} = \begin{pmatrix} F_{k_0}^{in} \\ F_{-k_0}^{in} \end{pmatrix} - \frac{i\Gamma/2}{v_g k_0 - \omega_e + i\frac{\gamma_{in}}{2} + i\frac{\Gamma}{2}(1 + e^{ik_0 d} \cos \phi)} \begin{pmatrix} 1 + \cos(k_0 d - \phi) & e^{-ik_0 d} (\cos k_0 d + \cos \phi) \\ e^{ik_0 d} (\cos k_0 d + \cos \phi) & 1 + \cos(k_0 d + \phi) \end{pmatrix} \begin{pmatrix} F_{k_0}^{in} \\ F_{-k_0}^{in} \end{pmatrix}. \quad (\text{S41})$$

From above formula we see that there is no reflection for input photons with wavenumber $\pm k_0$ if the phase ϕ satisfies $\cos(k_0 d) + \cos(\phi) = 0$. Equivalently, this leads to the condition

$$\phi = \phi_{L(R)} = \pi + (-)k_0 d, \quad (\text{S42})$$

where $\phi_{L(R)}$ leads to a left(right) chirality. Suppose that we consider photon on resonance with the field corresponding $\omega_e = v_g |k_0| + \frac{1}{4}\Gamma \sin(2k_0 d)$ and $\phi = \phi_R$. Then the scattering matrix is given by

$$\begin{pmatrix} F_{k_0}^{out} \\ F_{-k_0}^{out} \end{pmatrix} = \begin{pmatrix} 1 - \frac{2 \sin^2(k_0 d)}{\epsilon + \sin^2(k_0 d)} & 0 \\ 0 & 1 \end{pmatrix} \begin{pmatrix} F_{k_0}^{in} \\ F_{-k_0}^{in} \end{pmatrix}, \quad (\text{S43})$$

where we have introduced $\epsilon = \gamma_{in}/\Gamma$. The circulator fidelity to the right F_R is then

$$F_R = \left| \frac{\sin^2(k_0 d)}{\epsilon + \sin^2(k_0 d)} \right|^2 \approx 1 - 2\epsilon \sin^{-2}(k_0 d), \quad (\text{S44})$$

where in the second equality we have assumed that $\epsilon \ll 1$. The circulator fidelity has the optimal point $1 - 2\epsilon$ at $k_0 d = \pi/2$. Recall that the operation frequency of our chiral interface can be tuned in a band of a few GHz. If the circulator works at $k_0 d = 0.8 \times \pi/2$, the fidelity reads $\approx 1 - 2.103\epsilon$, which is not much different from the optimum point.

The above calculation shows that the fidelity is limited by the ratio $\epsilon = \gamma_{in}/\Gamma$. Indeed, superconducting circuit is superior to other platforms of waveguide QED in terms of lossless ϵ . As an example, in the experiment of Ref. [S3], the transmon Q-1 has $\gamma_{in}/2\pi = 430\text{kHz}$ and $\Gamma/2\pi = 94.1\text{MHz}$, hence $\epsilon = 0.0046$ and $\max_{\omega} F_R = 0.991$. Even better results are feasible for other transmon parameters. For example, in a recent experiment [S9], a transmon with lateral size larger than 500 micrometers is fabricated, and found to have a coherence time exceeding 0.3ms, i.e., an inherent loss rate of about $\gamma_{in}/2\pi \sim 3\text{kHz}$, yielding a negligible infidelity.

-
- [S1] J. Koch, A. A. Houck, K. L. Hur, and S. M. Girvin, Time-reversal-symmetry breaking in circuit-qed-based photon lattices, *Physical Review A* **82**, [10.1103/physreva.82.043811](#) (2010).
- [S2] J. Koch, T. M. Yu, J. Gambetta, A. A. Houck, D. I. Schuster, J. Majer, A. Blais, M. H. Devoret, S. M. Girvin, and R. J. Schoelkopf, Charge-insensitive qubit design derived from the cooper pair box, *Phys. Rev. A* **76**, [042319](#) (2007).
- [S3] M. Mirhosseini, E. Kim, X. Zhang, A. Sipahigil, P. B. Dieterle, A. J. Keller, A. Asenjo-Garcia, D. E. Chang, and O. Painter, Cavity quantum electrodynamics with atom-like mirrors, *Nature* **569**, [692](#) (2019).
- [S4] B. Kannan, M. J. Ruckriegel, D. L. Campbell, A. F. Kockum, J. Braumüller, D. K. Kim, M. Kjaergaard, P. Krantz, A. Melville, B. M. Niedzielski, A. Vepsäläinen, R. Winik, J. L. Yoder, F. Nori, T. P. Orlando, S. Gustavsson, and W. D. Oliver, Waveguide quantum electrodynamics with superconducting artificial giant atoms, *Nature* **583**, [775](#) (2020).
- [S5] A. Wallraff, D. I. Schuster, A. Blais, L. Frunzio, R.-S. Huang, J. Majer, S. Kumar, S. M. Girvin, and R. J. Schoelkopf, Strong coupling of a single photon to a superconducting qubit using circuit quantum electrodynamics, *Nature* **431**, [162](#) (2004).
- [S6] J. Braumüller, L. Ding, A. P. Vepsäläinen, Y. Sung, M. Kjaergaard, T. Menke, R. Winik, D. Kim, B. M. Niedzielski, A. Melville, and et al., Characterizing and optimizing qubit coherence based on squid geometry, *Physical Review Applied* **13**, [10.1103/physrevapplied.13.054079](#) (2020).
- [S7] R. Barends, J. Kelly, A. Megrant, D. Sank, E. Jeffrey, Y. Chen, Y. Yin, B. Chiaro, J. Mutus, C. Neill, P. O'Malley, P. Roushan, J. Wenner, T. C. White, A. N. Cleland, and J. M. Martinis, Coherent josephson qubit suitable for scalable quantum integrated circuits, *Phys. Rev. Lett.* **111**, [080502](#) (2013).
- [S8] D. Roy, C. M. Wilson, and O. Firstenberg, Colloquium: Strongly interacting photons in one-dimensional continuum, *Rev. Mod. Phys.* **89**, [021001](#) (2017).
- [S9] A. P. M. Place, L. V. H. Rodgers, P. Mundada, B. M. Smitham, M. Fitzpatrick, Z. Leng, A. Premkumar, J. Bryon, A. Vrajitoarea, S. Sussman, G. Cheng, T. Madhavan, H. K. Babla, X. H. Le, Y. Gang, B. Jäck, A. Geynis, N. Yao, R. J. Cava, N. P. de Leon, and A. A. Houck, New material platform for superconducting transmon qubits with coherence times exceeding 0.3 milliseconds, *Nature Communications* **12**, [10.1038/s41467-021-22030-5](#) (2021).